

---

## Printed Dielectrophoretic Electrode- Based Continuous Flow Microfluidic Systems for Particles 3D- Trapping

Challier Lylian <sup>1,\*</sup>, Lemarchand Justin <sup>2</sup>, Dreanno Catherine <sup>1</sup>, Jauzein Cecile <sup>3</sup>, Mattana Giorgio <sup>2</sup>, Meriguet Guillaume <sup>4</sup>, Rotenberg Benjamin <sup>4</sup>, Noël Vincent <sup>2,\*</sup>

<sup>1</sup> IFREMER Centre de Brest Laboratoire Détection Capteurs & Mesures Plouzane F-29280,, France

<sup>2</sup> Université de Paris Laboratoire ITODYS CNRS UMR 7086 Paris F-75013 , France

<sup>3</sup> IFREMER , Centre de Brest Dyneco Pelagos Plouzane F-29280 , France

<sup>4</sup> Sorbonne Université Physico-Chimie des Electrolytes et Nanosystèmes Interfaciaux PHENIX CNRS UMR 8234 Paris F-75005 ,France

\* Corresponding authors : Lylian Challier, email address : [lylian.challier@ifremer.fr](mailto:lylian.challier@ifremer.fr) ; Vincent Noël, email address : [vincentnoel@u-paris.fr](mailto:vincentnoel@u-paris.fr)

---

### Abstract :

Inkjet-printing is used to fabricate dielectrophoretic electrodes able to trap polystyrene (PS) microparticles as well as model planktonic cells. The possibility of rapid prototyping offered by inkjet-printing allows the rational design of microchannels with tailored electric field distributions experienced by the suspended particles, which in turn provides a handle to drive them towards target regions. Specifically, this goal is achieved using two facing substrates constituting the bottom and the top walls of the channel, with a pair of interdigitated electrodes previously patterned by inkjet-printing on each side. Influence of electrode polarization (magnitude and frequency of the input signal) is investigated both theoretically, by modeling the electric field distribution inside the channel, and experimentally using confocal fluorescence microscopy. The printed device is able to sort circulating PS particles as a function of their size, with diameters ranging from 0.5 to 5  $\mu\text{m}$ , as well as to separate planktonic species according to their composition (*Alexandrium minutum* versus *Prorocentrum micans*). This work paves the way for the development of large-area, microstructured dielectrophoretic electrodes able to separate the constituents of samples at flow rates up to 150  $\mu\text{L mn}^{-1}$ .

**Keywords** : dielectrophoretic transport, finite element modeling, inkjet-printing, microfluidics, plankton sorting

## 1. Introduction

The assessment of plankton responses to environmental change, in particular for phytoplankton communities,<sup>[1]</sup> is of high scientific importance and may have profound political and economic implications within the frame of global climate change. Global warming and ocean acidification have led to detectable impacts on marine ecosystems. However, specific consequences on the diversity and dynamics of phytoplankton communities are difficult to assess as illustrated by contradictory results reported in the literature.<sup>[2,3]</sup> Indeed, this requires on the one hand the analysis of volumes large enough to be representative and, on the other hand, the use of sensitive analytical methods that allow to identify and count species with sizes spanning 3 orders of magnitude. Nowadays, an efficient analytical methodology is the flow cytometry,<sup>[4]</sup> based on the autofluorescence of pigments or size-related criteria analysis (*forward scatter signal* and *side scatter signal*). However, for a non-spherical object (which is the case of many phytoplankton genera), the size measurement is influenced by their orientation during the detection, introducing a bias in the measure. This limit makes morphological distinction difficult, while it is a predominant criterion for the analysis of planktonic communities.<sup>[5,6]</sup> Flow cytometry remains limited to natural fluorescence properties of plankton and need fluorescent probes or stains to detect the smallest communities, whereas they differ in many other physico-chemical parameters.

Planktonic cells may be conveniently described, as a first approximation, as electrically neutral but polarizable particles and, as such, dielectrophoresis (DEP) is able to separate each constituting species towards a designated region of space. DEP refers to the transport of polarizable particles suspended in a liquid medium, induced by inhomogeneous oscillating electric fields.<sup>[7]</sup> Spherical particles with electrical permittivity different from that of the medium experience a dielectrophoretic force  $\vec{F}_{DEP}$  whose time-averaged value can be expressed as:

$$\langle \vec{F}_{DEP} \rangle = 2\pi r_p^3 \epsilon_m \Re\{f_{CM}\} \nabla E_{rms}^2 \quad (1)$$

Where  $r_p$  is the particles' radius,  $\epsilon_m$  is the absolute electrical permittivity of the liquid medium,  $\Re\{f_{CM}\}$  is the real part of the frequency-dependent Clausius-Mossotti (CM) factor and  $\nabla E_{rms}^2$  is the gradient of the mean square electric field.

While all spherical particles experience the same electric field gradients, their response to the latter crucially depends on both their size and composition via the CM factor, defined as:

$$f_{CM} = \frac{\tilde{\epsilon}_p - \tilde{\epsilon}_M}{\tilde{\epsilon}_p + 2\tilde{\epsilon}_M} \quad (2)$$

where  $\tilde{\epsilon}_p$  and  $\tilde{\epsilon}_M$  denote the complex, frequency-dependent electrical permittivity of the particle and the liquid medium, respectively. The permittivity of each phase is related to its electrical conductivity  $\sigma_i$  via:

$$\tilde{\epsilon}_i = \epsilon_i - j \frac{\sigma_i}{2\pi f} \quad (3)$$

with  $f$  the frequency and  $j^2 = -1$ . Importantly, Equation 2 and 3 indicate that  $\Re\{f_{CM}\}$  can be positive (thus leading to the so-called positive DEP, pDEP) or negative (negative DEP, nDEP) depending on the frequency, the permittivity but also the conductivity of the system constituents. pDEP forces drive particles towards regions of high electric field whereas nDEP move them towards regions of low electric fields. For non-spherical particles, which include most of the biological cells,  $\vec{F}_{DEP}$  depends on their orientation with respect to the electric field, an effect which can be captured by modifying the CM factor in Equation 2 to account for the

three possible axes of polarization.<sup>[8]</sup> Therefore, a given unicellular organism will experience a unique (in terms of direction and magnitude) dielectrophoretic force  $\vec{F}_{DEP}$  under an electric field gradient, according to its size, shape, permittivity and conductivity. One can then envisage sorting devices based on appropriate electric field gradient design, possibly also exploiting the fact that various species will display different crossover frequencies between the nDEP and pDEP regimes.<sup>[9]</sup>

Among the different DEP methods, eDEP (*electrode-based dielectrophoresis*) is the only one able to generate dielectrophoretic forces sufficiently large to enable the control of particles at high throughput (*i.e.* under large fluid flow rates), while working at low voltages and high frequencies to reduce parasitic phenomena such as electrochemical and electrothermal ones. eDEP has already proved its relevance for phytoplankton<sup>[10-13]</sup> and freshwater lipid-producing algae sorting.<sup>[14-17]</sup> At the same time, eDEP has been under continuous investigation for several years in the field of cell sorting applications. The accessibility to photolithographic processes that are under constant improvement in terms of resolution and pattern complexity has contributed to a large extent to the increase of the  $\vec{F}_{DEP}$  magnitude. Previous works highlighted the need for producing three-dimensional structures to further increase  $\vec{F}_{DEP}$ .<sup>[18-20]</sup> Alongside these advances related to micrometric (bio)particles sorting, nano-photolithography has allowed the realization of nanometric gaps between asymmetric electrodes leading to local  $\vec{F}_{DEP}$  able to transport particles as small as DNA strands and viruses ( $\approx 100$  nm).<sup>[21,22]</sup> All the aforementioned strategies demonstrate the possibility to produce finely tuned  $\vec{F}_{DEP}$  (in terms of magnitude and orientation) acting on moving objects, but at the cost of considerably increasing the system complexity and fabrication costs (extensive use of electron beam fabrication processes).<sup>[23]</sup>

Marine samples analysis requires the development of specific DEP-based sorting systems, *i.e.* device able to analyse relevant sample volumes within a few hours. Electrode geometry must be designed to ensure strong DEP forces and large electrode patterns must be used to reach

unprecedented analysis rates too. To develop large-area DEP electrodes, alternatives to electron beam-based fabrication processes have to be investigated. Printing techniques, and especially inkjet-printing, can be used to produce DEP electrodes on large scale substrates. Printing has been already used in combination with electron beam fabrication method<sup>[24]</sup> and only one publication has so far reported on screen printed DEP electrodes.<sup>[25]</sup> Besides the ability to fabricate large DEP electrode areas on any substrates, including flexible ones, the use of inkjet-printing allows the rapid testing of different electrodes patterns (digital printing technique).<sup>[26]</sup>

Very few DEP devices are based on inkjet-printed (IJP) electrodes. Tran et al. succeeded in sorting cells at low voltages using IJP electrodes, but irreversible electrode damages were observed as a consequence of the applied polarization.<sup>[27]</sup> Esfandyarpoura et al. overcame this issue by using an insulating-DEP (*i*DEP) configuration, covering the IJP electrodes with a dielectric protective layer.<sup>[28]</sup> However, even at the high voltages used in *i*DEP configuration (*i.e.*, from 100 to 200 V<sub>pp</sub>), electric field gradients were not intense enough to induce DEP forces able to compete with hydrodynamic forces induced by pressure gradients. Consequently, cell sorting was considered at a maximum flow rate of 1 μL/min, a throughput which is not adapted to marine samples analysis. Progress must be done regarding both the device design (*e.g.* electrodes location in the channel) and electrode printing quality (sharp edge, stability) to develop high-flow rate DEP devices dedicated to plankton sorting.

In the present work, we develop for the first time a methodology dedicated to the understanding of DEP transport processes combining electrodes fabrication by inkjet-printing, electric field distribution simulation and operando optical tracking of model latex particles. The goal is the development of a microfluidic device ensuring an optimal object trapping efficiency while maintaining short analysis duration (continuous flow) and allowing the control of the transport processes to convey all plankton of a given type in a dedicated (separation) and spatially restricted (accumulation) area for their subsequent counting. We

develop a microfluidic device containing printed Ag electrodes on flexible polyethylene naphthalate (PEN) substrates constituting the top and bottom channel sides. We correlate the particles accumulation area and their trapping efficiencies to the electric field distribution inside the whole microfluidic system with the help of finite element calculations. This unique approach to date leads to a better understanding of the dielectrophoretic processes and, most importantly, provides a way to control dielectrophoretic fluxes by tuning the device structure in terms of electrodes geometry and relative position. To practically demonstrate the relevance of our results, a proof of concept of inkjet-printed dielectrophoretic channel is also shown and its performances, in terms of plankton cells sorting and flow rate, are evaluated.

## 2. Results and discussion

The chip used for dielectrophoretic measurements is illustrated in **Figure 1**. The electrodes are inkjet-printed using a silver nanoparticles-based ink on a polyethylene naphthalene (PEN) substrate (Figure 1a). The top and bottom electrodes are then glued onto a polydimethylsiloxane (PDMS) substrate, whose thickness defines the channel height (Figure 1b). The chip is equipped with two holes (“inlet” and “outlet”, see Figure 1c and 1d) for connection with a microfluidic system, which makes it possible to control the flow rate of the analysed samples (see the Experimental Section and **Figure S11**, Supporting Information, for more details on the fabrication and assembly of the chip).

Figure 1e depicts a parallelized version of the device where 16 identical couples of electrodes are connected to increase water flow.

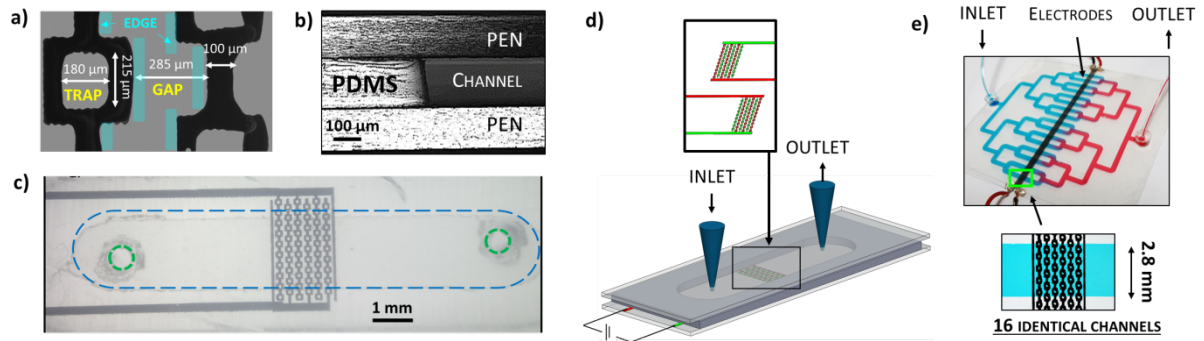


**Figure 1.** (a) Picture of the inkjet-printed Ag pattern; (b) Side view picture showing that the channel height is fixed by the PDMS layer thickness embedded between two PEN substrates. (c) top view picture ( $\times 60$ ) of the device (dashed line: zone in contact with the liquid sample), (d) Schematic representation of the bottom electrodes configuration implemented in a microfluidic system; (e) 16 Parallel identical channels of 2.8 mm width and 180  $\mu\text{m}$  height.

In the following sections, the different experiments performed on the chip are presented and the corresponding results are interpreted and discussed.

## 2.1. Coplanar interdigitated electrodes

The magnitude of the DEP force is proportional to the gradient of the square of the local electric field (see Equation 1). This gradient can be enhanced without increasing the applied voltage by using asymmetric electrodes. In such attempt, interdigitated Ag electrodes made of connected square rings were printed on PEN (see Figure 1a).<sup>[29]</sup> The unitary structure is thus composed of a sequence of equipotential square traps separated by a gap from another sequence of identical squares at a different electric potential. The main advantage of this structure is to present a highly asymmetrical geometry and especially to allow the accumulation of particles on a substrate area which is not covered by the Ag electrodes so that it is particularly easy to image the particles by means of optical microscopy. By using a bulk electrode or another PEN substrate onto which interdigitated electrodes are printed as a top cover, many configurations were investigated. For clarity, we note as  $x$ ,  $y$  and  $z$  the position along the main axis, the cross section and the height of the channel respectively. All the

investigated configurations are composed of the repetition of elementary units (see **Figure 2**) both in terms of polarity and pattern. In the following, coordinates will be expressed as a fraction of this elementary cell, *e.g.*  $x = y = z = 1/2$  is located at the centre of the elementary cell.

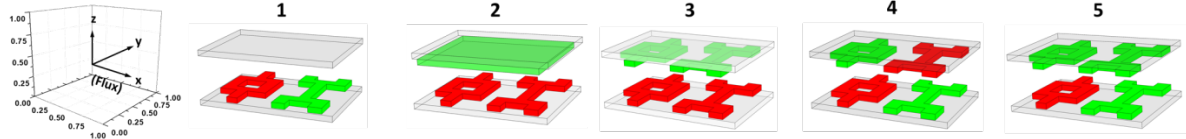


**Figure 2.** Schematic representation of the device architectures. Colours illustrate the electrode polarity (red :  $+V$ , green:  $-V$ ).

We first used finite element calculations method to map the electric field distribution throughout the device for configuration 1, *i.e.* only one pair of interdigitated electrodes located at  $z = 0$  (the channel bottom). Figure 3a shows the distribution of  $E^2$  in this plane. We can identify two types of regions corresponding to local minima of  $E^2$  where particles should accumulate in the nDEP regime: global minima (corresponding to the equilibrium positions) at the centre of the traps, and local minima in the gap (corresponding to wider metastable basins from which particles should eventually escape to reach the global minima). In the pDEP regime, particles should accumulate in areas corresponding to the maxima of  $E^2$ , *i.e.* on the outer edges of the square traps. The map of  $E^2$  in the planes parallel to the electrodes one but located at different heights ( $z = 1/2, z = 1$ ; see Figures 3b and 3c) shows the presence of a minimum located above every printed pattern, around  $x=1/4$  and  $3/4$ . However, as underlined by the distribution of  $E^2$  in the  $(x,z)$  plane at  $y = 1/2$  (see Figure 3d), the electric field intensity decreases sharply from the bottom to the top plane.



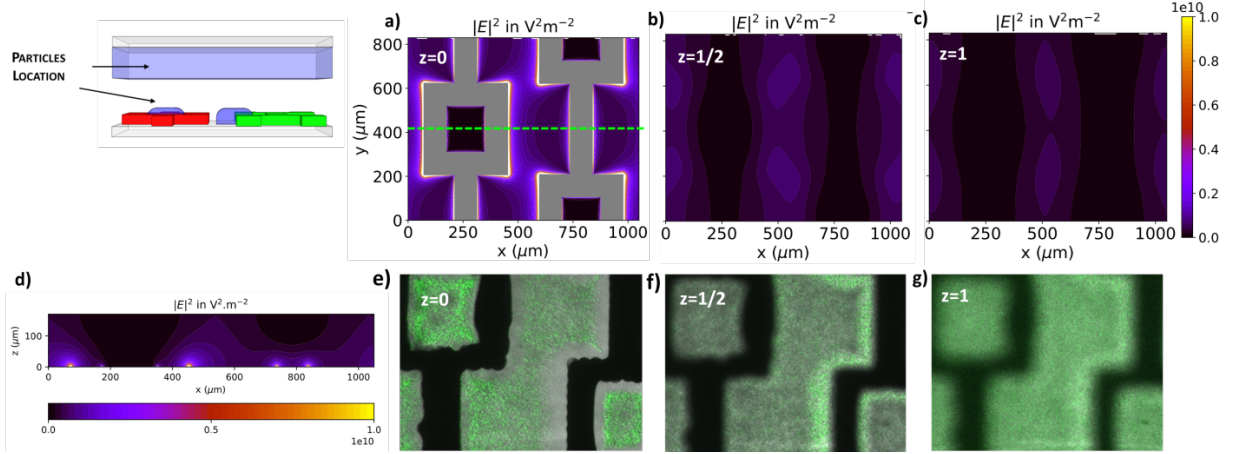


**Figure 3.** Calculated distribution of  $E^2$  in (a). bottom part of the channel plane, (b) in the channel mid-plane, (c) near the top of the channel. (d) Cross section (green dashed line in Fig. 3a); Pictures after 60 s polarization at 20  $V_{pp}$  (10 MHz) of PS particles ( $d = 1 \mu m$ ) (e) in the plane of the electrodes ( $z=0$ ), (f) at mid-channel ( $z=1/2$ ) and (g) in the upper part of the channel ( $z=1$ ). *Note:* Shaded purple zones in the top-left scheme depict the particle trapped by the dielectrophoretic forces.

Polystyrene particles of  $1 \mu m$  in diameter were studied first in the absence of flux. We notice that the particles do not precipitate over the duration of the experiments. The application of a sinusoidal electric field of 20  $V_{pp}$  causes a flow of particles for all the studied frequencies (from 1 kHz to 10 MHz). For frequencies lower than 1 kHz, Ag electrodes undergo electro-dissolution, which is responsible for the appearance of both disconnections and even unwanted short circuits, as silver redeposits around its point of dissolution (data not shown). For frequencies from 1 kHz to 10 kHz, the particles exhibit convective motions (Figure SI2, and video SI, Supporting Information) consistent with electroosmotic processes.<sup>[30, 31]</sup>

As the frequency is increased, DEP forces dominate leading to particles accumulation in high and low field zones depending on the used frequency.<sup>[31]</sup> For frequencies ranging from 10 kHz to *ca.* 2.1 MHz, particles are attracted towards the edge of the electrode that corresponds to high fields zones (pDEP, Figure 4a). For frequencies from 2.1 MHz to 10 MHz, particles accumulate in the gap and in the trap, *i.e.* they are repelled from high field zones (nDEP, Figure 4b).

The particle dielectrophoretic behaviour can be predicted through the modelling of the  $\Re\{f_{CM}\}$  variation as a function of the frequency. Such a calculation requires the estimation of the particle conductivity ( $\sigma_p$ ) that can be deduced from the crossover frequency. Indeed, for a spherical particle subjected to a single interfacial relaxation process, the Maxwell-Wagner crossover frequency  $f_{c.o}$  is defined by Equation 4.<sup>[32]</sup>

$$f_{c.o} = \frac{(\sigma_p + 2\sigma_m)}{2\pi\epsilon_0(\epsilon_p + 2\epsilon_m)} \quad (4)$$

$$\text{with } \sigma_p = \sigma_{p,bulk} + 2 \cdot \frac{K_s}{r_p} \quad (5)$$

where  $K_s$  is the particle surface conductance.<sup>[29]</sup> Taking  $\epsilon_m = 78\epsilon_0$ ,  $\epsilon_p = 2.55\epsilon_0$ ,  $\sigma_m = 2.8 \cdot 10^{-3} \text{ S m}^{-1}$  and  $f_{c.o} = 2.1 \text{ MHz}$ ,  $\sigma_p$  is deduced from Equation 4 ( $12,9 \times 10^{-3} \text{ S m}^{-1}$ ). Note that considering  $\sigma_{p,bulk} = 6,7 \times 10^{-14} \text{ S m}^{-1}$  and  $r_p = 0.5 \mu\text{m}$ , a  $K_s$  of ca. 3.22 nS is estimated from Equation 5, a value in close accordance with the literature.<sup>[33,34]</sup> Knowing  $\sigma_p$ , the variation of  $\Re\{f_{CM}\}$  as a function of the frequency can be plotted (see Figure 4c).

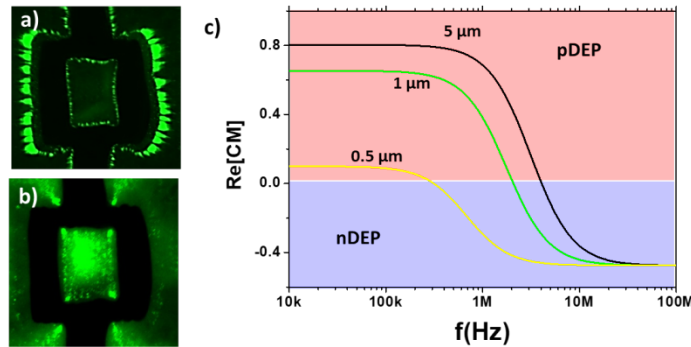


**Figure 4.** Pictures of the bottom electrodes plane after 120 s polarization at 20  $V_{pp}$  for fluorescent PS particles with diameter 1.1  $\mu\text{m}$  at (a) 100 kHz and (b) 10 MHz, (c) Calculated real part of the Clausius-Mossotti factor,  $\Re\{f_{CM}\}$ , for  $\epsilon_m = 78\epsilon_0$ ,  $\epsilon_p = 2.55\epsilon_0$ ,  $\sigma_m = 2.8 \times 10^{-3} \text{ S m}^{-1}$ ,  $\sigma_{p,bulk} = 6.7 \times 10^{-14} \text{ mS m}^{-1}$ ,  $K_s = 6 \times 10^{-9} \text{ S}$ ,  $d = 5 \mu\text{m}$  (black line),  $d = 1 \mu\text{m}$  (green line),  $d = 500 \text{ nm}$  (yellow line).

The zones identified from the numerical calculations as of strong and weak electric fields are in excellent agreement with the experimental observations of pDEP and nDEP transport (see

Figure 3a). For the rest of this work, we only investigated the nDEP regime at 10 MHz, on the one hand to ensure pure dielectrophoretic transport (neither electroosmotic nor electrochemical phenomena) and on the other hand to assess the size-sorting ability of the device with respect to the electrodes configuration (see section 2.3), frequency being another possible parameter for further optimization.

An important feature of the device is its ability to accumulate objects regardless of their initial position in the channel, especially along the direction perpendicular to the electrodes plane. Figure 3f and 3g show pictures respectively at the mid-channel plane and near the top of the channel. It appears that many particles remain randomly distributed above the mid-channel plane in accordance with the  $E^2$  distribution, which displays almost no electric field gradient in that region (see Figure 3d).

## **2.2 Top-bottom electrodes configuration**

One way to achieve the control of DEP transport processes in the entire channel is to control the electric potential on both sides of the channel. To achieve this goal, the previous configuration has been modified by using an ITO/Au electrode as the upper part of channel, the pair of interdigitated electrodes constituting its lower part being equipotential (configuration 2, see Figure 2). The results obtained are qualitatively identical to the previous configuration with a significant accumulation in the plane of the bottom interdigitated electrodes, mainly inside the traps and in the gaps (see Figure SI3, Supporting Information). However, the distribution of  $E^2$  is much more anisotropic than for configuration 1, leading to a significantly larger density of accumulated particles for the same applied voltage and frequency. Nevertheless, a homogeneous particle distribution in the upper part of the channel is again noted, consistently with the distribution of the field strength  $E^2$  showing an almost constant value above the channel mid-plane. Thus, even though the configuration 2 the electric field is felt throughout the channel, the gradient is too weak to allow accumulation, except for the particles already present in the lower half of the channel.

To increase the anisotropy of the electric field while maintaining strong gradients in the  $z$  direction, two printed substrates were positioned on each side of the channel (the so-called top-bottom interdigitated electrodes configuration, *cf.* configurations 3-5 in Figure 2). For configuration 3, the distribution of particles upon the application of the sinusoidal field changes noticeably compared to the previously investigated configurations. There are no more particles in the mid-channel, as they are all concentrated inside the traps and the gaps of both the bottom and the top electrode planes (see Figure 5a). The particles are efficiently concentrated in the nDEP areas as depicted by the  $E^2$  distribution in the planes of the electrodes (see Figure 6a). The absence of particles in the mid-channel plane despite the presence of a  $E^2$  minimum in the  $(x,y)$  plane located on the top of gaps ( $x = z = 1/2$ ) results from field gradients in the  $z$  direction, as discussed below.

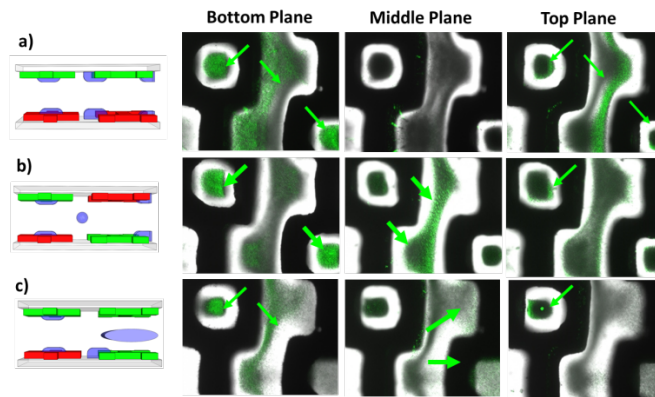


**Figure 5.** Pictures after 60 s polarization at 20 V<sub>pp</sub> (10 MHz) of PS particles ( $d = 1 \mu\text{m}$ ) of (from left to right) the bottom ( $z = 0$ ), mid- ( $z = 1/2$ ) and top ( $z = 1$ ) channel planes corresponding to the configuration (a) 3, (b) 4 and (c) 5. *Note:* Shaded zones in the schemes depict the particle trapped by the dielectrophoretic forces.

The configuration 4 (a *quadrupole-like* configuration) accumulates the particles in the traps of both the top and the bottom electrode planes. But here, as opposed to the previous studies architectures, the gap is empty (see Figure 5b) and another marked difference is the accumulation of particles in the mid-channel plane, within an area located at the very centre from each of the 4 electrodes ( $x = z = 1/2$ ).

In a first approximation, as depicted in **Figure 6**, the  $E^2$  distribution has the same features for the configurations 3 and 4, namely deep nDEP zones constituted by the electrode traps. However, a close examination reveals subtle differences in the electric field distribution in the gap. Indeed, in some cases, the nDEP zones have the shape of continuous valleys along the  $y$ -direction (see Type A in Figure 6), while in others these nDEP zones also display saddle points ( $E^2$  barriers along the valley) located near trap corners (see Type B in Figure 6). It seems that particles experiencing nDEP transport only accumulate in the Type A gaps, *i.e.* in the gap of the bottom and top electrodes planes of configuration 3 and in the mid-channel plane of configuration 4.

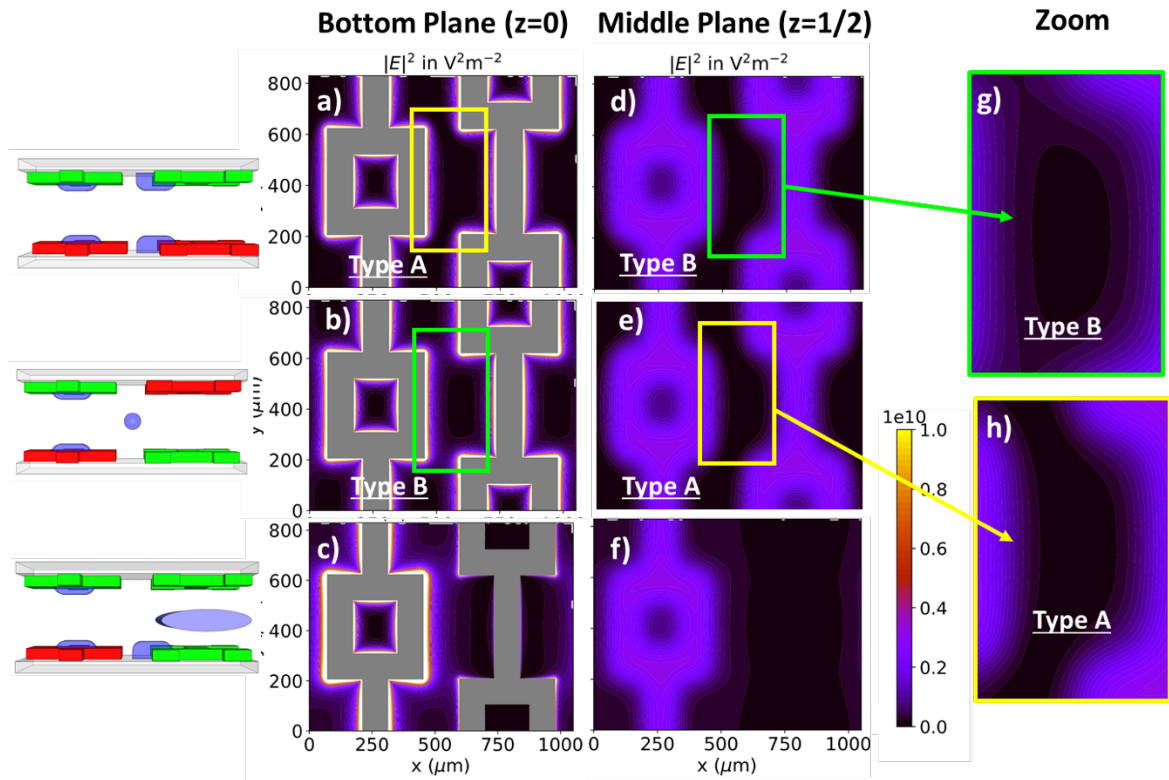


**Figure 6.** Distribution of  $E^2$  in (from left to right) the bottom ( $z = 0$ ) and the mid- ( $z = 1/2$ ) channel planes for the configurations 3 (panels a and d), 4 (b and e) and 5 (c and f). (Top-electrodes related data are shown in Figure SI4, Supporting Information). g) Zones displaying  $E^2$  minimum valleys separated by saddle points (type B) and h) Zones displaying a continuum of  $E^2$  minimum (type A).

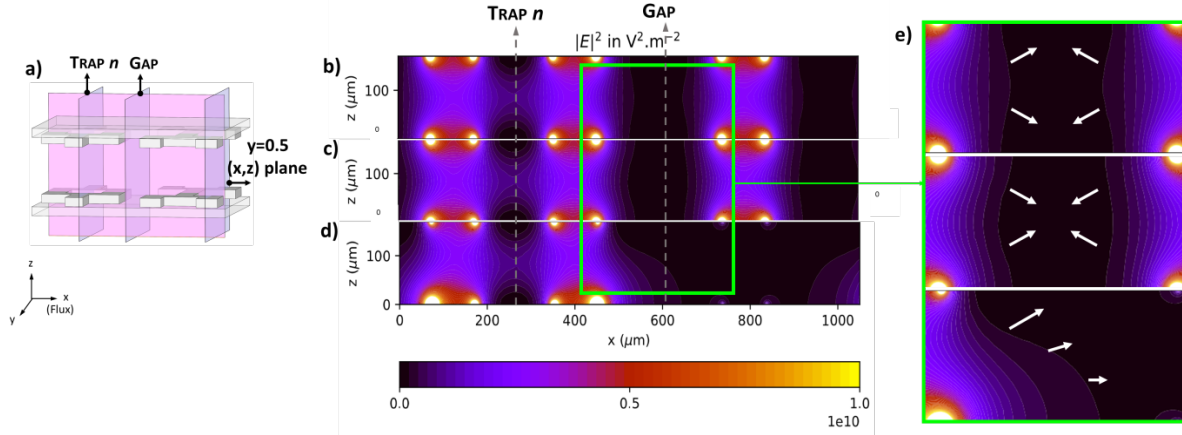


**Figure 7.** (a) Sections along which the field is mapped in the other panels. Cross section of  $E^2$  distribution at  $y = 400 \mu m$  for configurations 3 (panel b), 4 (c) and 5 (d). Panel (e) shows a zoom of the region indicated in green on the central panel, centred at  $x = 600 \mu m$ , revealing the fine structure of the  $E^2$  distribution; white arrows depict the direction of nDEP forces.

Other processes acting in the  $z$  channel direction can also be anticipated as central in the observed distribution pattern. **Figure 7** shows the  $E^2$  distribution in the  $z$  direction and allows a direct understanding of the capacity of configurations 3 and 4 to drive particles respectively in the gap of the electrode planes and at the centre of the channel. For both configurations, there is a broad low  $E^2$  region located on the top of the gaps ( $400 \mu m < x < 800 \mu m$ ). However, a close examination indicates that DEP forces direction (see arrows in zooms of Figure 7e), defined by the gradient of  $E^2$  should be different between configurations 3 and 4 with a resulting dielectrophoretic transport respectively towards the electrode planes ( $z = 0, z = 1$ ) and towards the mid-channel plane ( $z = 1/2$ ).

Configuration 5, with three equipotential electrodes, clearly illustrates this capability to control the location of accumulation zones as well as their extension. Indeed, accumulation zones are localized inside the traps of the two facing electrodes having different potentials (see Figure 5c), a pattern already observed for the configuration 1, but the presence of a broad region of low field strength  $E^2$  between the other two facing electrodes identically polarized (see Figure 6c and 7d) also leads to accumulation of particles in the middle of the channel

### 2.3 Trapping efficiency under pressure-driven flow

Under pressure-driven flow, the particles circulate in a laminar hydrodynamic regime and are therefore subject to a thrust parallel to the channel main axis that decreases radially from the centre to the channel edges. Such force has a noticeable impact on the particle trajectory and hence the location of accumulation areas. For the configuration 3, the competition between the thrust and the DEP forces leads to a distribution of particles that depends on the position in the interdigitated electrodes network. Almost no particles with a diameter of  $1\ \mu\text{m}$  are trapped in the first interdigitated electrodes, and the trapping increases along the flow direction (see Figure 8b).

Before discussing the effect of the particle size, we first observe that, unexpectedly, the particles tend to align into discrete parallel lines crossing each trap in its middle. This is better seen on Figure 8e, which provides a zoom of the region framed in panel 8b and shows that particles are progressively driven by nDEP towards the low electric field gradient regions. This can be understood by considering the distribution of  $E^2$  in the channel cross section, *i.e.* the  $(y,z)$  plane, in particular along the  $y$ -direction of the electrodes, as illustrated in **Figure 9** (for  $x = 0.25$ ). It is obvious from this figure that in the nDEP regimes particles will be driven towards regions located above the traps corresponding to lower fields, and as a result focussed as they flow in the  $x$ -direction. Note that such  $E^2$  distribution is obtained for all the configurations (*i.e.*, 3 to 5, see Figure SI5, Supporting Information).

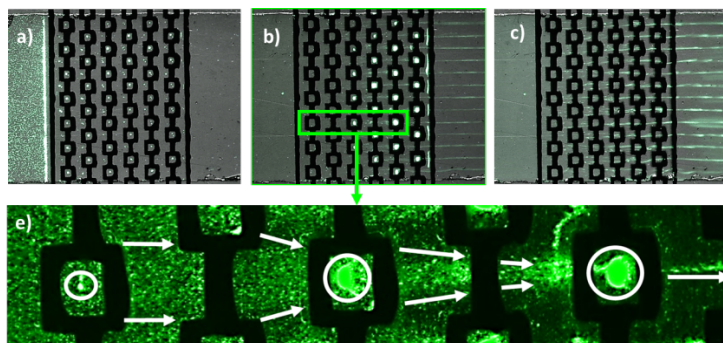


**Figure 8.** Pictures after 20 min of polarization at 20 Vpp (10 MHz) at  $1 \mu\text{l mn}^{-1}$  of latex particles (a)  $d = 5 \mu\text{m}$ , (b)  $d = 1 \mu\text{m}$  and (c)  $d = 0.5 \mu\text{m}$ . (d) zoom on a section of Figure 8b; white arrows depict the particle focalization process driven by nDEP and thrust forces.

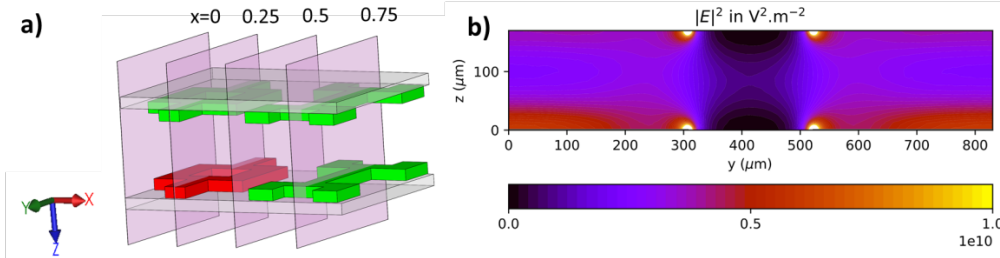


**Figure 9.** (a) scheme depicting the  $x$ -position the considered  $(y, z)$  planes. (b)  $E^2$  distribution in the  $(y, z)$  plane at  $x = 0.25$  in the configuration 5.

Since the DEP driving force scales with the particle volume (see Equation 1), we investigated the effect of particle size using additional PS beads of 0.5 and 5  $\mu\text{m}$  of diameter (see Figure 8a and 8c). The DEP force acting on 5  $\mu\text{m}$  particles is so strong that the particles fail to cross the first barrier of  $E^2$ , *i.e.* the first electrode line, whereas only a few particles are still observed in the classical nDEP zones (trap and gap). On the contrary, most 0.5  $\mu\text{m}$  particles cross the electrodes without significant accumulation. As for 1  $\mu\text{m}$  particles, large streaks are visible at the outlet of the electrode area. Moreover, when the frequency is switched to 100 kHz, *i.e.* in pDEP condition for 0.5  $\mu\text{m}$  particles ( $\Re\{f_{CM}\} = 0.8$ ), these particles streaks disappear (Figure SI6, Supporting Information), thus further confirming that it is the nDEP force that leads to the observed focalization.

The difference in accumulating patterns can be explained in terms of the net force acting on each particle. Indeed, particles trajectory mostly depends on the combination of the thrust force (along the flow, *i.e.* in the  $x$ -direction) and the DEP force (mainly perpendicular to the flow, *i.e.* in the  $y$ - and  $z$ -directions). Depending on the relative magnitude of these forces, a given particle may fall in a  $E^2$  minimum located near the first electrodes series (DEP regime),



as observed for particles with diameter is larger than  $0.5\ \mu\text{m}$ , or proceed through the channel with a ballistic trajectory (pressure-driven flow regime, see **Figure 10**).

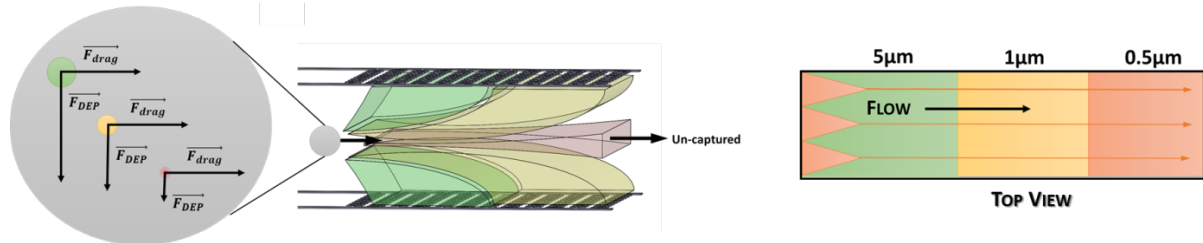


**Figure 10.** Schematic representations of particles trajectory as a function of their size. The coloured regions in the right panel depict the accumulation zones according to the size of the particles.

In this respect, the comparison of the configurations 3 to 5 makes it possible to study the influence of the geometry of the electrodes on the retention capacity. For all these configurations, the accumulation of particles is observed at the same locations as those identified in the absence of flow, except at the centre of the channel (configurations 4 and 5) which is empty due to the drag forces. Particle retention capacity was estimated using flow cytometry (see Experimental Section). For  $5\ \mu\text{m}$  particles, retention rate were  $> 99\%$ , for flow rate up to  $5\ \mu\text{l min}^{-1}$ . For  $1\ \mu\text{m}$  particles, retention of *ca.*  $43\%$ ,  $22\%$  and  $58\%$  was obtained for the configuration 3-5 respectively. Hence, the configuration 5 shows the best trapping efficiency, in accordance with the  $E^2$  distribution. Besides the trapping efficiency, configuration 5 allows the accumulation of targets in more restricted areas compared to all the other studied cases.

## 2.4 Ability of the device to sort plankton cells

To illustrate our device ability to sort plankton cells, two model algae, *Alexandrium minutum* (*AM*) and *Prorocentrum micans* (*PM*) were investigated using configuration 5, which provides the best retention efficiency under flow. These two microalgae were selected for their similar dimensions ( $d = 20$  to  $30\ \mu\text{m}$ , see **Table 1**).

**Table 1** : Morphological characteristics of *AM* and *PM* algae.

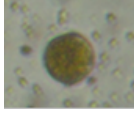
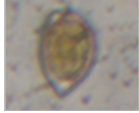
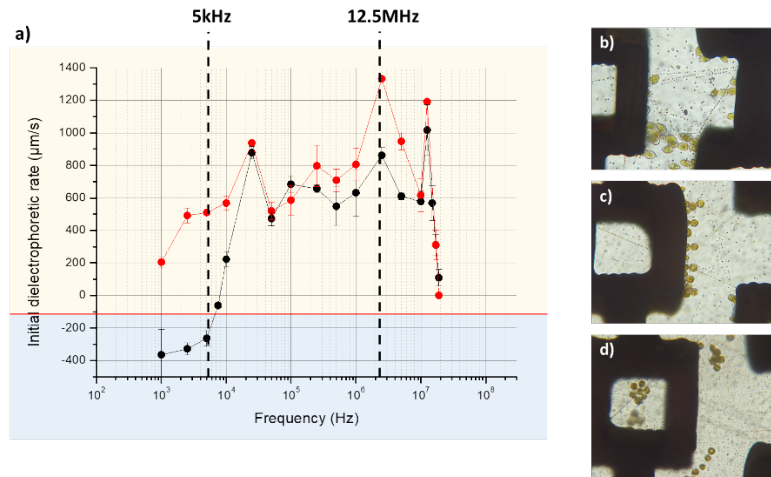
	<b>Alexandrium minutum</b>	<b>Prorocentrum micans</b>
<b>Cell picture under isosmotic low conductivity media</b>		
<b>Shape</b>	Spherical ellipsoid	Flattened ellipsoid
<b>Dimension (<math>\mu\text{m}</math>) <math>\pm 10\%</math></b>	21 $\times$ 29	33 $\times$ 21 $\times$ 17
<b>Biovolume <math>\mu\text{m}^3</math></b>	3594 $\pm$ 23%	6193 $\pm$ 15%

Figure 11a shows the initial dielectrophoretic velocity of each microalgae, measured when applying an electric field ( $20 V_{pp}$ ,  $f > 1$  kHz) without flow, as a function of the electric field frequency. Under these conditions, the algae velocity is proportional to the DEP force and their direction depends on the sign of  $\Re\{f_{CM}\}$  (see Equation 1).

In Figure 11a the negative and positive initial dielectrophoretic velocity refers to pDEP and nDEP respectively. The variation of the initial velocity with frequency for *AM*, which has a spheroidal geometry, has a classical feature with an approximate crossover frequency of 8 kHz. Above this frequency, the *AM* cells experience pDEP transport and below a nDEP one. *PM* experiences only pDEP transport on the explored frequency range. The dielectrophoretic velocity measurements are in total accordance with the distribution of both species after 60 s of polarization. Indeed, at 12.5 MHz, both *AM* and *PM* accumulate in pDEP zones (see Figure 11b and 11c) whereas at 5 kHz, only *AM* accumulate in nDEP areas (see Figure 11d).



**Figure 11.** (a) Initial DEP velocity for *AM* (black line) and *PM* (red line) for  $E = 20V_{pp}$  and  $1\text{kHz} < f < 20\text{ MHz}$ . Pictures after 60s polarization at  $20 V_{pp}$  of (b) *PM* trapped in pDEP area at 10 MHz (c) *AM* trapped in pDEP area at 10 MHz and (d) *AM* trapped in nDEP area at 5 kHz.

An equicellular mixture of *AM* and *PM* ( $10^3\text{ cells ml}^{-1}$ ) has been introduced within the chip (configuration 5,  $20 V_{pp}$ ). The flow rate was increased gradually until cells could not be trapped, corresponding to a critical rate of  $10\ \mu\text{l min}^{-1}$ . Therefore, a frequency of 12.5MHz was applied for 30 min allowing algae cells to accumulate in the first pDEP area they encountered, meaning the first electrode finger (see Figure 12a and 12b). Then, the frequency was switched to 5kHz, a frequency leading to pDEP and nDEP transport for *PM* and *AM*, respectively. As soon as the frequency is set to 5 kHz, *AM* cells accumulated at the first electrode are released, repelled from the edge (high electric field gradient) of the electrode by nDEP (Figure 11b), while *PM* cells remain trapped by pDEP (Figure 12d). *AM* cells are then driven by the flow and nDEP force, leading to an accumulation in the next electrode gap (Figure 12e). These results demonstrate the possibility to separate cells under continuous flow thanks to this electrode configuration.

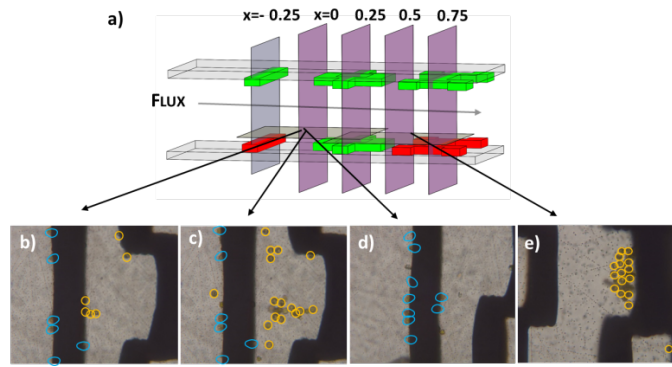


**Figure 12.** (a) Position along  $x$  of the considered  $(y, z)$  cross-sections. (b)  $PM$  (surrounded with a blue line) and  $AM$  (surrounded by an orange line) trapping at  $20 V_{pp}$  and  $12.5 \text{ MHz}$  after  $10 \text{ min}$  (c) Release of  $AM$  cells at  $20 V_{pp}$  and  $5 \text{ kHz}$  (d) Purified  $AM$  cells in a low  $E^2$  area at  $x = 0.75$ .

### 2.5 Device Scale-up: towards high throughput algae analysis

Thanks to the use of printing methods, the DEP electrodes patterns can be directly sized-up by creating parallel channels. We designed and printed a large electrode pattern covered by a specifically designed PDMS film creating a 16-parallel channel DEP device in which all the channels have the same dimension, i.e.  $180 \mu\text{m}$  of height and  $2.8 \text{ mm}$  of width (see Figure 1f). The flow is laminar throughout the microfluidic device, the flow rate being proportional to the number of channels involved at a given position between inlet and outlet (see Figure SI 7, Supporting Information).  $9 \text{ mL}$  of  $AM$  suspension ( $3,000 \text{ cells ml}^{-1}$ ) at flow rate of  $150 \mu\text{L mn}^{-1}$  were analysed using a frequency of  $12.5 \text{ MHz}$  ( $20 V_{pp}$ ). Under these conditions, the device succeeds in trapping  $AM$  algae in the pDEP zones already identified (*i.e.*, edge of electrodes and gap between interdigitated ones). To the best of our knowledge, this result is beyond the state-of-the-art since previously published DEP devices worked under flow rates below  $100 \mu\text{L mn}^{-1}$ .<sup>[31,32]</sup>

### 3. Conclusion

Putting two pairs of interdigitated electrodes facing each other, *i.e.* on both the lower and on the upper part of the channel makes it possible to investigate many configurations as the two

pairs of electrodes can be polarized in various ways. By modelling the electric field distribution for each electrodes configuration, we deciphered their dielectrophoretic behaviour and achieved a fine understanding of the relationships between the device geometry and  $\vec{F}_{DEP}$  which can be directly used in the future development of plankton sorting devices. On the one hand, investigation of model polystyrene microparticles demonstrates the device capability in terms of size-based sorting. On the other hand, we succeeded in sorting algae having the same dimensions but having a different dielectric behaviour (variability of the algae constituents). These results clearly demonstrate the possibility of using printed electrodes for plankton separation. Printing fabrication technologies allow the production of DEP devices on large areas and and to trap plankton at a high flow rate ( $150 \mu\text{L}\cdot\text{mn}^{-1}$ ). The main challenge now is the fabrication of printed patterns capable of generating electric field gradients strong enough to separate and accumulate particles of dimensions  $0.2\text{-}1 \mu\text{m}$ , i.e. the picoplankton. This work is ongoing and will be published in a forthcoming paper.

#### **4. Experimental Section**

*Chemicals:* Sucrose, Bovine serum albumin (BSA) and 3-aminopropyltriethoxysilane (APTES) were purchased from Sigma-Aldrich. The poly(dimethylsiloxane) (PDMS) (Sylgard 184) and curing agent were purchased from Dow Corning. Polystyrene microspheres of different diameters ( $0.5, 1$  and  $5 \mu\text{m}$ ) were purchased from Thermo Scientific.

*Algae culture:* *Alexandrium minutum* (AM) and *Porocentrum micans* (PM) were cultured in f/2 media. The recipe consists in mixing filtered sea water and five stocks solutions ( $\text{NaNO}_3$  solution,  $\text{NaH}_2\text{PO}_4$  solution, trace metal solution, vitamin solution and  $\text{Na}_2\text{SiO}_3$  solution).

During the culture period, algae were exposed to a cycle of 12 hours of light and 12 hours of dark at  $\sim 20^{\circ}\text{C}$  in an environmental chamber (Strader, France). Algal suspensions concentrations were estimated with a Malassez haemocytometer counting-cell.

*Dielectrophoretic prototype fabrication:* Electrodes were fabricated on polyethylene naphthalate (PEN) foils (Teonex® Q65, 125  $\mu\text{m}$  thick). Prior to any printing, PEN foils were sonicated for 5 minutes in acetone followed by 5 more minutes of sonication in ethanol. After cleaning, the substrates were dried with argon and then dehydrated for at least 1 hour at 180  $^{\circ}\text{C}$  in a convection oven. Commercial silver-nanoparticles ink (PV-Nanocell I40DM-106) with 40% metal by weight was used for printing the silver electrode arrays. The printer used was a Dimatix Fujifilm DMP-2800™ with 10 pL drops cartridges; the drop spacing was set to 25  $\mu\text{m}$  and the platen temperature at 40 $^{\circ}\text{C}$ . The curing and sintering of the ink were performed in a convection oven at 180  $^{\circ}\text{C}$  for 1 h in an air atmosphere. The minimal electrode width was in the range from 90 to 150  $\mu\text{m}$  with approximately 300 nm in height. Electrode spacing was set to 180  $\mu\text{m}$  (see Figure 1a). The final pattern presents interdigitated electrodes covering an area of ca. 1 cm  $\times$  3 mm. For the 16 channel device (Figure 1e), the same printing procedure was used to obtain a layout with a length of 9 cm.

For the device configuration with the Ag electrodes array facing a planar gold electrode, ITO coated polyethylene terephthalate (PET) sheets (60  $\Omega \text{ sq}^{-1}$ , Sigma Aldrich) were used. First of all, a strip of adhesive tape (5  $\times$  20 mm) is applied onto the ITO surface. Then, the non-protected ITO is chemically etched with 1% HCl solution, to reveal the underlying PET substrate to allow bonding with the PDMS. In a third step, PET is protected with tape, and ITO is covered with a thin film of gold (15 nm thickness) using a Balzers SCD 040 sputtering system (Switzerland) at a constant voltage of 2000 V and current of 15 mA during 90 s. Finally, the tape is removed, and the substrate is cleaned with ethanol.

The multilayered structure of the chip consists in a PDMS membrane (180  $\mu\text{m}$  thick) between two substrates with printed electrodes or ITO/Au electrode. First, the PDMS membrane is prepared by spin-coating of 1 g of uncured PDMS on polytetrafluoroethylene (PTFE) tape (500 rpm, 30s), glued on clean microscope glass slides. To ensure a homogeneous membrane in height, the PDMS is cured by placing the microscope glass slide in a Petri dish, floating in a bath set to 80°C. After 1 hour, the bilayer [PTFE/PDMS] is removed from the microscope glass slide and the channel (4 mm  $\times$  24mm) is obtained with a leather punch (see Figure SI1a, Supporting Information). To improve the adhesion of the PDMS to the PEN (see Figure SI1b, Supporting Information), the surface of the latter is oxidized 5 minutes in a UV/O<sub>3</sub> cleaner (UVO-CLEANER Model 42 series, Jelight Company Inc, USA) and then placed in an aqueous solution of 2% v/v APTES for at least 20 minutes. This step allows the PEN surfaces to bond a pre-activated side of the PDMS (5 minutes in a UV/O<sub>3</sub>). The triple layers [PTFE/PDMS]/PEN are then placed one hour in an oven at 60°C. After this step, the PTFE tape is pulled off. The second side of the PDMS is activated 5 minutes in the UV/O<sub>3</sub> ozone cleaner and the top electrodes are aligned with the bottom electrode under a stereo microscope (Stemi 508, Zeiss, Germany). The three-layer device [PEN/PDMS/PEN] is then placed at least one hour in an oven at 60°C. Finally, electric connections are ensured with silver conductive epoxy (Chemtronics, USA) protected with resin epoxy glue after drying.

For the fabrication of the 16 parallel channels, a 180  $\mu\text{m}$ -thick PDMS layer was spincoated (500 rpm for 20s) on a PEN substrate previously cut into a 17.5 cm diameter circle. The microfluidic pattern was obtained using a vinyl plotter Roland Camm-1 GS-G24 with high precision blade (175  $\mu\text{m}$  offset).

*Dielectrophoretic experiments:* Experiments with Polystyrene (PS) microspheres were performed in an aqueous medium with a conductivity of  $\sigma_m = 2.8 \cdot 10^{-3} \text{ S m}^{-1}$ . Particles of 5  $\mu\text{m}$  diameter were used at  $1 \times 10^7$  particles  $\text{ml}^{-1}$  whereas particles of 1 and 0.5  $\mu\text{m}$  diameters were

used at  $1.10^8$  particles  $\text{ml}^{-1}$ . For DEP experiments with *AM* and *PM*, 10 ml of algae culture were centrifuged for 3 minutes at 3500 rpm. The supernatant was removed and the pellet was suspended in a 1M sucrose solution. This technique permits performing DEP experiments at both low conductivity and isosmotic pressure.

The inlet of particles and algae suspension was realized with an *Ismatec Reglo ICC* peristaltic pump, allowing a flow rate varying from  $0.2 \mu\text{l min}^{-1}$  to  $1 \text{ ml min}^{-1}$ . AC voltage was applied between the electrode arrays in a microfluidic channel with an arbitrary waveform generator DG1022 (RIGOL, China). The amplitude ( $20 V_{\text{PP}}$ ) and frequency (from 1kHz to 20 MHz) of the applied signal were simultaneously measured with an oscilloscope Wavejet 312, (LeCroy, USA).

Images and videos were recorded through a Diavert Inverted Trinocular microscope (Leitz Wetzlar, Germany) combined with an Axiocam 105 colour (Zeiss, Germany). To measure the translational velocity of  $5 \mu\text{m}$  particles and algae, the video acquired is decomposed frame by frame using the open-source video analysis program *Physmo*. This software permits exporting objects displacement in a  $(x, y)$  plane. Considering the camera frame rate (fps) and the pixel calibration (using USAF 1951 resolution test chart) velocities were extracted from the video. To evaluate the 3D trapping efficiency of the devices, confocal images of fluorescent PS particles were taken with an Apotome Axio Imager Z with a COLIBRI system or Axio Zoom.V16 (Zeiss, Germany) depending on the magnification needed. Equipment from Zeiss was controlled by the Zen software. The model particle retention rate was estimated using a Cytosense automated flow cytometer (Cytobuoy, Netherlands). For planktonic cell trapping at high throughput with the 16 parallel-channel device, the channels were previously passivated using a  $1\text{g L}^{-1}$  BSA solution in order to limit cells adsorption.

*Modelling:* In order to compute the distribution of the mean square of the electric field  $E^2$  inside the device, we solved the Poisson equation by assuming that the fluid is electrically



neutral. This is expected to be a good approximation away from the electrodes (*i.e.* beyond the electric double layer, which does not extend beyond a few nm at high electrolyte concentrations), which we validated *a posteriori* thanks to the excellent agreement of the results with the experimental observations. The electrostatic potential  $V(x,y,z)$  then satisfies  $\Delta V = 0$ , with  $\Delta$  the Laplacian operator, with boundary conditions corresponding to the prescribed value at the surface of each electrode (either 0 or 10 V depending on the polarity) and to a vanishing surface charge on the other parts of the walls. This equation is solved numerically for each geometry and polarity by finite element calculations using the COMSOL Multiphysics software.<sup>[35]</sup> The electric field is then computed as the gradient  $\vec{E} = -\vec{\nabla}V$  and the colour maps in the figures indicate the square of the norm of this field. More precisely, the geometry of the electrodes is described (with simulated dimensions) on the experimental image on Fig. 1a. The channel height (distance between the bottom and top substrates) is taken as 170  $\mu\text{m}$ , while the height of the electrodes (on each substrate) used in the calculations is 1  $\mu\text{m}$ . All results presented for the "bottom" and "top" planes correspond to the field distribution in the mid-plane of the electrodes, *i.e.* a distance from the substrates of 0.5 and 169.5  $\mu\text{m}$ , respectively (even though they are referred to, for simplicity, as  $z = 0$  and  $z = 1$  in reduced units, in the following). Periodic boundary conditions are used in the directions parallel to the substrates ( $x$  and  $y$ ), but not in the perpendicular direction ( $z$ ).

### **Supporting Information**

Supporting Information is available from the Wiley Online Library or from the author.

### **Acknowledgements**

The authors want to thank the FABLAB of the University of Bretagne Occidentale (the OPENFACTORY) for their advice in PDMS layer cutting. J. L. thanks the ED 388 for his PhD grant.

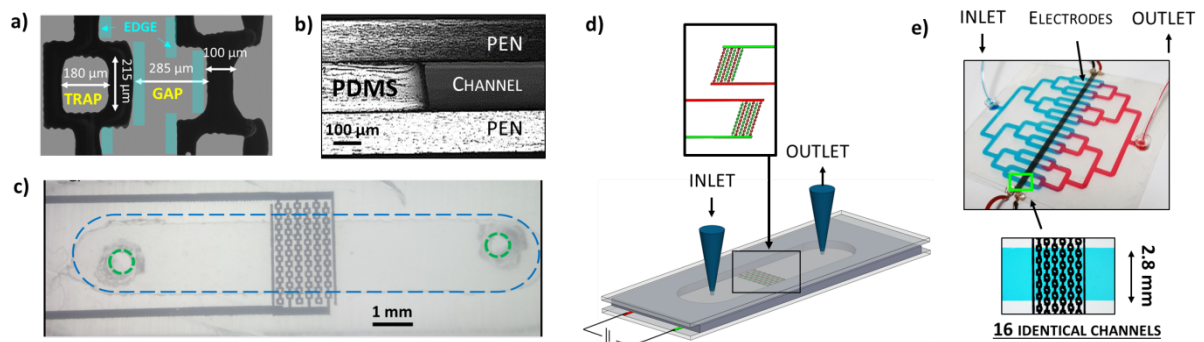
Received: ((will be filled in by the editorial staff))  
Revised: ((will be filled in by the editorial staff))  
Published online: ((will be filled in by the editorial staff))

## References

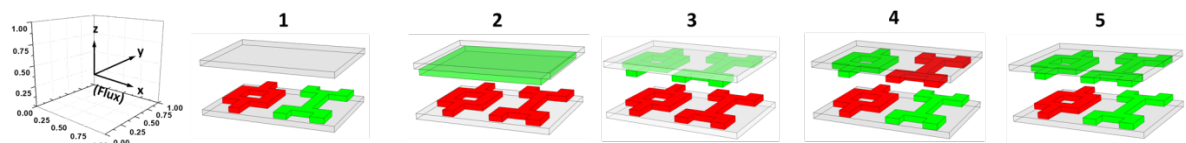
- [1] J.-P. Gattuso, A. Magnan, R. Billé, W. W. L. Cheung, E. L. Howes, F. Joos, D. Allemand, L. Bopp, S. R. Cooley, C. M. Eakin, O. Hoegh-Guldberg, R. P. Kelly, H.-O. Pörtner, A. D. Rogers, J. M. Baxter, D. Laffoley, D. Osborn, A. Rankovic, J. Rochette, U. R. Sumaila, S. Treyer, C. Turley, *Science* **2015**, 349, aac4722.
- [2] L. Maugendre, C. Guieu, J.-P. Gattuso, F. Gazeau. *Estuarine, Coastal and Shelf Science* **2017**, 186, 1.
- [3] F. Gazeau, A. Sallon, P. Pitt, A. Tsiol, L. Maugendre, M. Gianie, M. Celussie, M. L. Pedrotti, S. Marro, C. Guieu, *Estuarine, Coastal and Shelf Science* **2017**, 186, 72.
- [4] B.S Lambert, R. J. Olson, H. M. Sosik, *Limnol. Oceanogr. Methods* **2017**, 15, 94.
- [5] L. Roselli, E. Litchman, E. Stanca, F. Cozzoli, A. Basset, *J. Plankton Res.* **2017**, 39, 577.
- [6] E. Stanca, M. Cellamare, A. Basset, *Hydrobiologia* **2012**, 701, 99.
- [7] H. A. Pohl, H. Pohl, *Dielectrophoresis: the behavior of neutral matter in nonuniform electric fields*, Cambridge University Press, Cambridge, UK, **1978**.
- [8] H. Morgan, N. G. Green, *J. Electrostat.* **1999**, 42, 279.
- [9] B. Yafouz, N. A. Kadri, F. Ibrahim, *Sensors* **2014**, 14, 6356.
- [10] R. T. K. Kumar, P. Kanchustambham, D. Kinnamon, S. Prasad, *Algal Res.* **2017**, 27, 109.
- [11] S. Bunthawin, R. J. Ritchie, P. Wanichapichart, *J. Sci. Technol.* **2011**, 33, 585.
- [12] C. Siebman, O. D. Velev, V. I. Slaveykova, *Biosensors* **2017**, 7, 4.
- [13] C. Sussillon, O. D. Velev, V.I. Slaveykova, *Biomicrofluidics* **2013**, 7, 024109.
- [14] A. R. Schor, C. R. Buie, *Int. Mechanical Engineering Congress and Exposition*, Houston, TX, USA, November **2012**.
- [15] H. Hadady, D. Redelman, S. R. Hiibel, E. J. Geiger, *AIMS Biophysics*, **2016**, 3, 398.

- [16] Y.-L. Deng, J.-S. Chang, Y.-J. Juang, *Bioresource Technol.* **2013**, 135, 137.
- [17] Y.-L. Deng, M.-Y. Kuo, Y.-J. Juang, *Biomicrofluidics* **2014**, 8, 064120.
- [18] J. Voldman, M. L. Gray, M. Toner, M. A. Schmidt, *Anal. Chem.* **2002**, 74, 3984.
- [19] C. Iliescu, G. Tresset, G. Xu, *Biomicrofluidics* **2009**, 3, 044104.
- [20] L. Wang, L. A. Flanagan, N. L. Jeon, E. Monuki, A. P. Leeac, *Lab on a Chip* **2007**, 7, 1114.
- [21] M. Viefhues, R. Eichhorn, *Electrophoresis* **2017**, 38, 1483.
- [22] N. A. Rahman, *Sensors* **2017**, 17, 449.
- [23] P. Chen, Y.-Y. Huang, G. Bhave, K. Hoshino, X. Zhang, *Ann. Biomed. Eng.* **2016**, 44, 1710.
- [24] S.H. Lee, G. Yun, Y. Koh, *Micro and Nano Syst. Lett.* **2013**, 5, 1.
- [25] H. Zhu, X. Lin, Y. Su, H. Dong, J. Wu, *Biosens. Bioelectron.* **2015**, 63, 371.
- [26] G. Mattana, A. Loi, M. Woytasik, M. Barbaro, V. Noël, B. Piro, *Adv. Mater. Technol.* **2017**, 2, 1700063.
- [27] V.-T. Tran, Y. Wei, W. J. Liao, H. Yang, H. Du, *Micromachines*, **2017**, 8, 106.
- [28] R. Esfandyarpour, M. J. DiDonato, Y. Yang, N. G. Durmus, J. S. Harris, R. W. Davis, *PNAS*, **2017**, 114, E1306.
- [29] S. Park, M. Koklu, Ali Beskok, *Anal. Chem.* **2009**, 81, 2303.
- [30] T. Honegger, K. Berton, E. Picard, D. Peyrade, *Appl. Phys. Lett.* **2011**, 98, 181906.
- [31] W.M. Arnold, U. Zimmermann, *J. of Electrostat.* **1988**, 21, 151.
- [32] S. K. Ravula, D. W. Branch, C. D. James, R. J. Townsend, M. Hill, G. Kaduchak, M. Ward, I. Brener, *Sensors Actuat. B-Chem.* **2008**, 130, 645.
- [33] Y. Wu, Y. Ren, Y. Tao, L. Hou, H. Jiang, *Anal Chem.* **2018**, 90, 11461.
- [34] N. Gadish, J. Voldman, *Anal Chem.* **2006**, 78, 7870.
- [35] COMSOL Multiphysics® v. 5.0. www.comsol.com. COMSOL AB, Stockholm, Sweden.

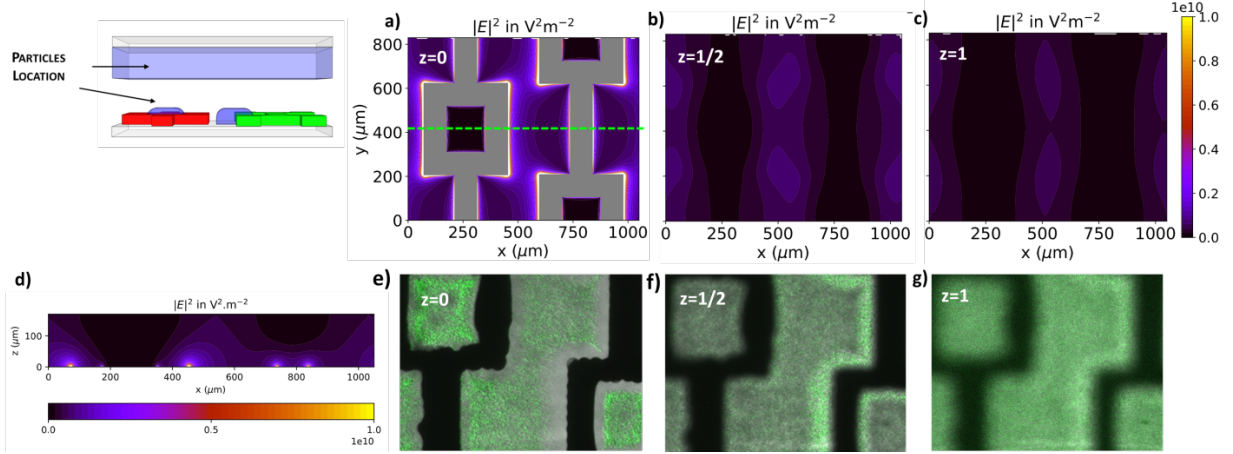
## List of Figures



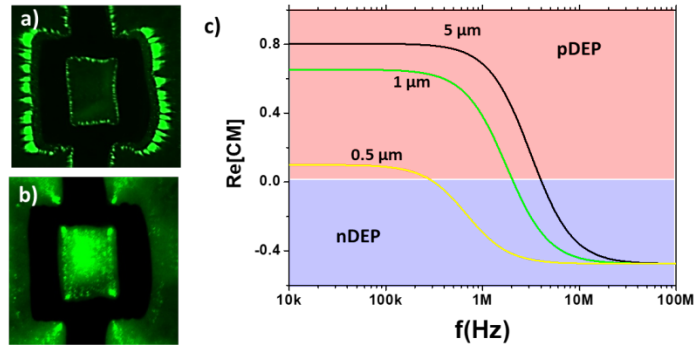
**Figure 2.** (a) Picture of the inkjet-printed Ag pattern; (b) Side view picture showing that the channel height is fixed by the PDMS layer thickness embedded between two PEN substrates. (c) top view picture ( $\times 60$ ) of the device (dashed line: zone in contact with the liquid sample), (d) Schematic representation of the bottom electrodes configuration implemented in a microfluidic system; (e) 16 Parallel identical channels of 2.8 mm width and 180  $\mu\text{m}$  height.



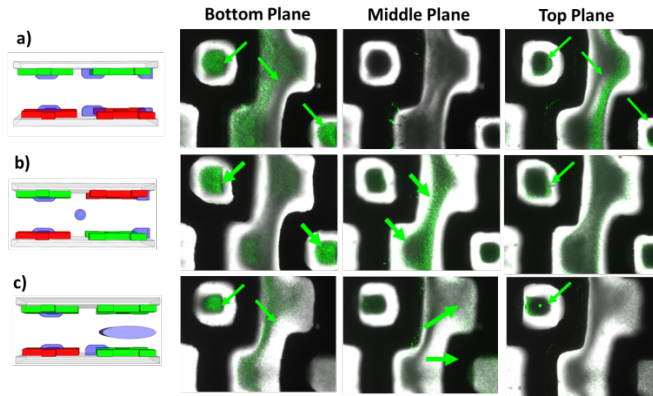
**Figure 2.** Schematic representation of the device architectures. Colours illustrate the electrode polarity (red :  $+V$ , green:  $-V$ ).



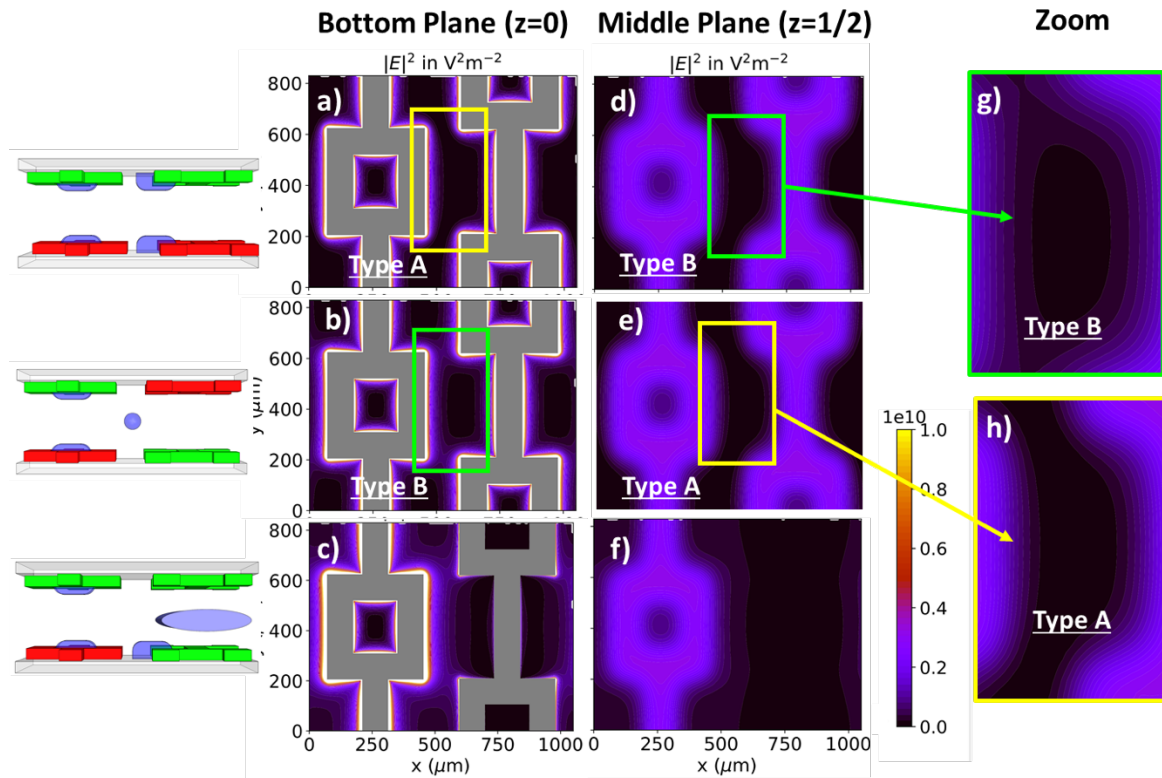
**Figure 3.** Calculated distribution of  $E^2$  in (a). bottom part of the channel plane, (b) in the channel mid-plane, (c) near the top of the channel. (d) Cross section (green dashed line in Fig. 3a); Pictures after 60 s polarization at 20  $V_{pp}$  (10 MHz) of PS particles ( $d = 1 \mu\text{m}$ ) (e) in the plane of the electrodes ( $z=0$ ), (f) at mid-channel ( $z=1/2$ ) and (g) in the upper part of the channel ( $z=1$ ). *Note:* Shaded purple zones in the top-left scheme depict the particle trapped by the dielectrophoretic forces.



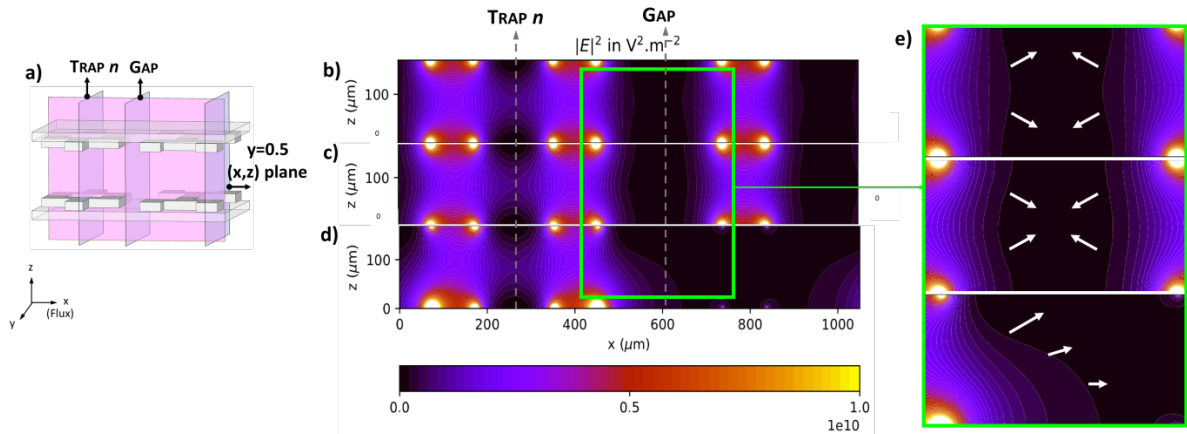
**Figure 4.** Pictures of the bottom electrodes plane after 120 s polarization at 20  $V_{pp}$  for fluorescent PS particles with diameter 1.1  $\mu\text{m}$  at (a) 100 kHz and (b) 10 MHz, (c) Calculated real part of the Clausius-Mossotti factor,  $\Re\{f_{CM}\}$ , for  $\epsilon_m = 78\epsilon_0$ ,  $\epsilon_p = 2.55\epsilon_0$ ,  $\sigma_m = 2.8 \times 10^{-3} \text{ S m}^{-1}$ ,  $\sigma_{p,bulk} = 6.7 \times 10^{-14} \text{ mS m}^{-1}$ ,  $K_s = 6 \times 10^{-9} \text{ S}$ ,  $d = 5 \mu\text{m}$  (black line),  $d = 1 \mu\text{m}$  (green line),  $d = 500 \text{ nm}$  (yellow line).



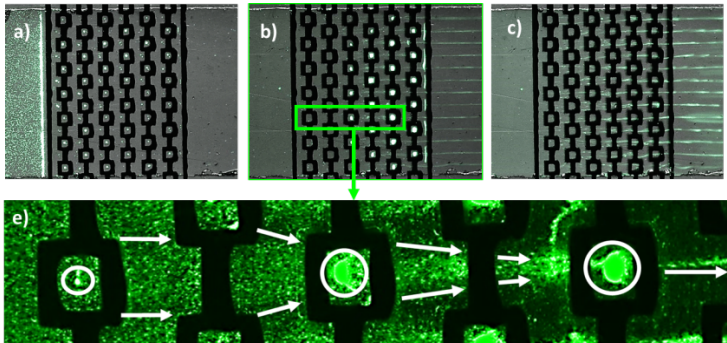
**Figure 5.** Pictures after 60 s polarization at 20 V<sub>pp</sub> (10 MHz) of PS particles ( $d = 1 \mu\text{m}$ ) of (from left to right) the bottom ( $z = 0$ ), mid- ( $z = 1/2$ ) and top ( $z = 1$ ) channel planes corresponding to the configuration (a) 3, (b) 4 and (c) 5. *Note:* Shaded zones in the schemes depict the particle trapped by the dielectrophoretic forces.



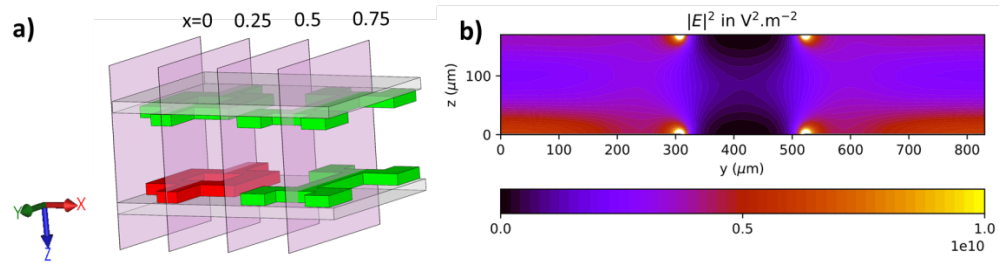
**Figure 6.** Distribution of  $E^2$  in (from left to right) the bottom ( $z = 0$ ) and the mid- ( $z = 1/2$ ) channel planes for the configurations 3 (panels a and d), 4 (b and e) and 5 (c and f). (Top-electrodes related data are shown in Figure SI4, Supporting Information). g) Zones displaying  $E^2$  minimum valleys separated by saddle points (type B) and h) Zones displaying a continuum of  $E^2$  minimum (type A).



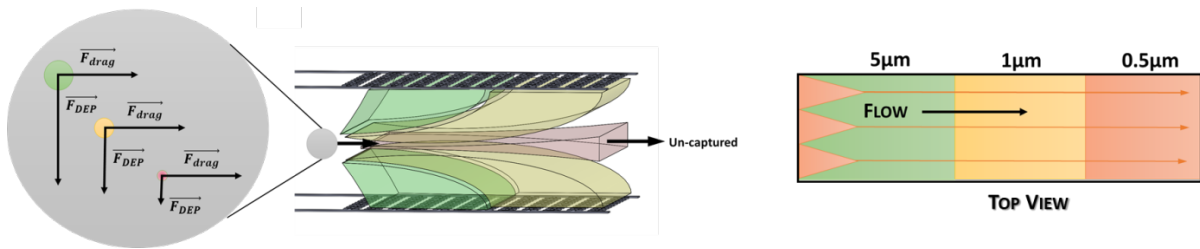
**Figure 7.** (a) Sections along which the field is mapped in the other panels. Cross section of  $E^2$  distribution at  $y = 400 \mu\text{m}$  for configurations 3 (panel b), 4 (c) and 5 (d). Panel (e) shows a zoom of the region indicated in green on the central panel, centred at  $x = 600 \mu\text{m}$ , revealing the fine structure of the  $E^2$  distribution; white arrows depict the direction of nDEP forces.



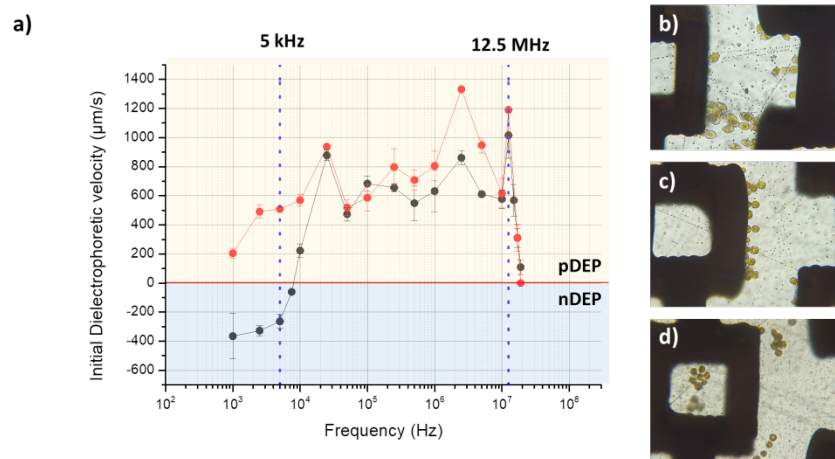
**Figure 8.** Pictures after 20 min of polarization at 20 Vpp (10 MHz) at  $1 \mu\text{l mn}^{-1}$  of latex particles (a)  $d = 5 \mu\text{m}$ , (b)  $d = 1 \mu\text{m}$  and (c)  $d = 0.5 \mu\text{m}$ . (d) zoom on a section of Figure 8b; white arrows depict the particle focalization process driven by nDEP and thrust forces.



**Figure 9.** (a) scheme depicting the x-position the considered  $(y, z)$  planes. (b)  $E^2$  distribution in the  $(y, z)$  plane at  $x = 0.25$  in the configuration 5.

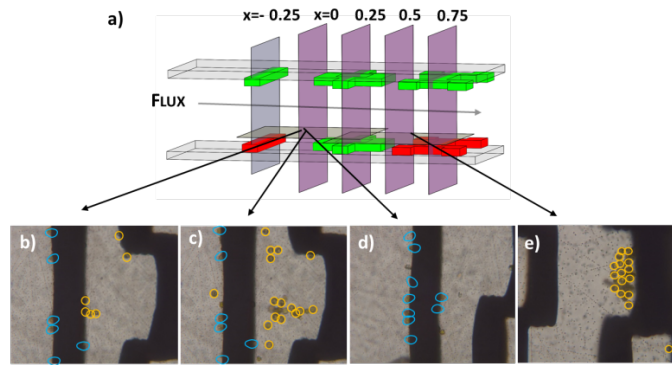


**Figure 10.** Schematic representations of particles trajectory as a function of their size. The coloured regions in the right panel depict the accumulation zones according to the size of the particles.



**Figure 11.** (a) Initial DEP velocity for AM (black line) and PM (red line) for  $E = 20V_{pp}$  and  $1kHz < f < 20$  MHz. Pictures after 60s polarization at 20  $V_{pp}$  of (b) PM trapped in pDEP area at 10 MHz (c) AM trapped in pDEP area at 10 MHz and (d) AM trapped in nDEP area at 5 kHz.

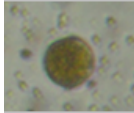





**Figure 12.** (a) Position along  $x$  of the considered  $(y, z)$  cross-sections. (b) *PM* (surrounded with a blue line) and *AM* (surrounded by an orange line) trapping at 20  $V_{pp}$  and 12.5 MHz after 10 min (c) Release of *AM* cells at 20  $V_{pp}$  and 5 kHz (d) Purified *AM* cells in a low  $E^2$  area at  $x = 0.75$ .

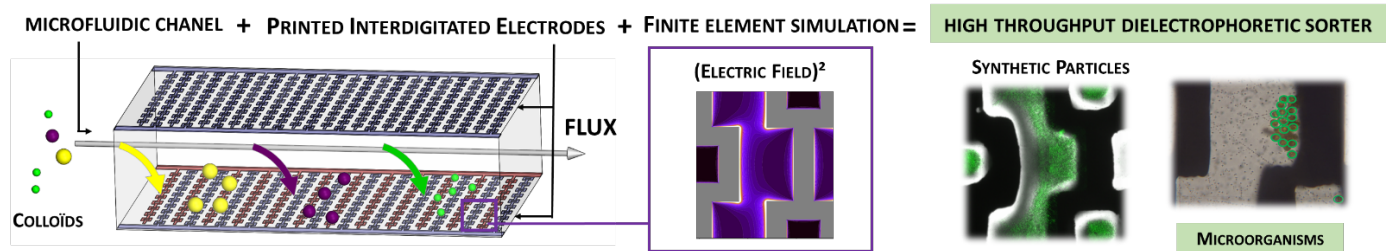
## List of Tables

**Table 1 :** Morphological characteristics of *AM* and *PM* algae.

	<b>Alexandrium minutum</b>	<b>Prorocentrum micans</b>
<b>Cell picture under isosmotic low conductivity media</b>		
<b>Shape</b>	Spherical ellipsoid	Flattened ellipsoid
<b>Dimension (<math>\mu\text{m}</math>) <math>\pm 10\%</math></b>	21×29	33×21×17
<b>Biovolume <math>\mu\text{m}^3</math></b>	3594±23%	6193±15%

The table of contents entry should be 50–60 words long, and the first phrase should be bold.

**Printed dielectrophoretic electrodes coupled to microfluidics are used to drive colloids** toward a given channel location according to their size (500 nm to 5 μm-radius polystyrene nanoparticles) and their chemical composition (*Alexandrium minutum* vs *Prorocentrum micans* planktons) at high flow rate. The device architecture is designed by tailoring the electric field distribution with numerical modelling and fabricated by inkjet-printing.



*Full page TOC Figure*

# Printed Dielectrophoretic Electrode-based Continuous Flow Microfluidic Systems for particles 3D-Trapping

L. Challier, J. Lemarchand, C. Dreanno, C. Jauzein, G. Mattana, G. Mériguet, B. Rotenberg, V. Noel

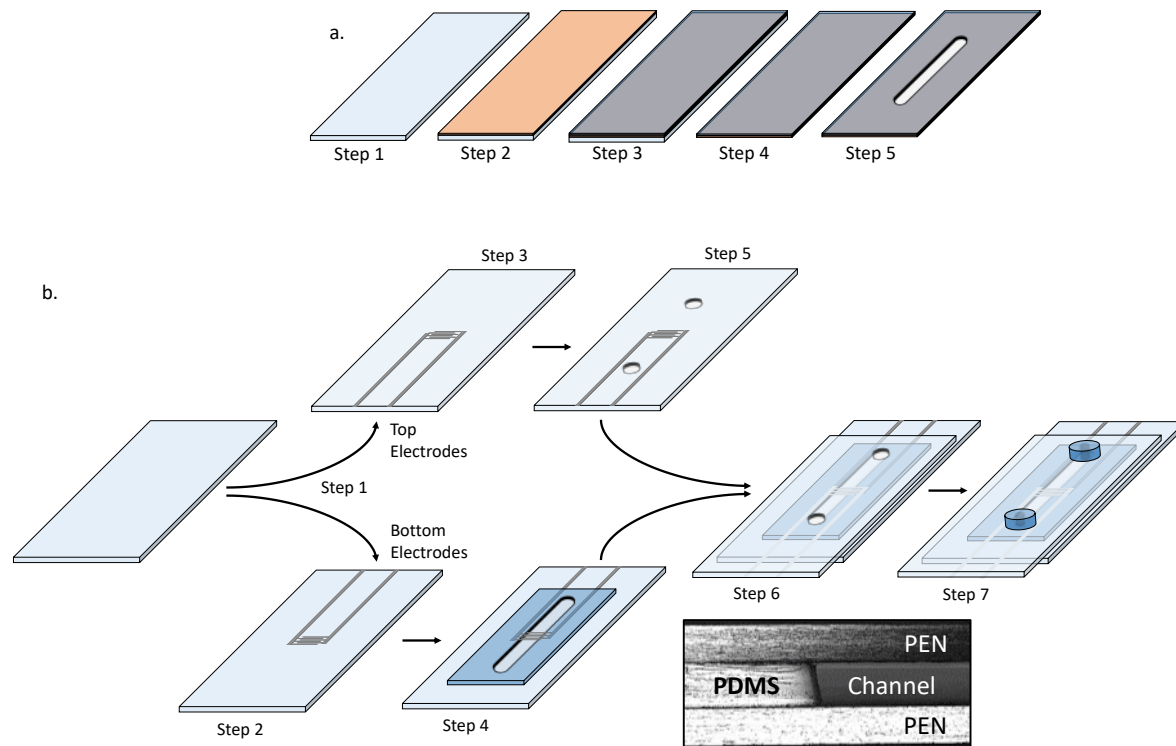


**Fig. S11** (a) PDMS membrane preparation. Step 1: Substrate cleaning; Step 2: PTFE tape bonding; Step 3: PDMS spin coating and curing; Step 4: PTFE/PDMS release; Step 5: microfluidic channel punched. (b). Top Bottom Electrodes chip fabrication. Step 1: PEN substrate cleaning and electrode printing; Step 2/3: UV/O<sub>3</sub> treatment 5 min and 30 min immersion in APTES 2% / H<sub>2</sub>O; Step 4: PDMS membrane activation with UV/O<sub>3</sub> during 5 min and transfer on the bottom electrode substrate; Step 5: Hole punching for inlet and outlet; Step 6: Electrode alignment and bonding of the two parts; Step 7: UV/O<sub>3</sub> treatment 5 min and 30 min immersion in APTES 2%/H<sub>2</sub>O for Microfluidic connection bonding. The photography is a cross section of the channel at the edge of the PDMS

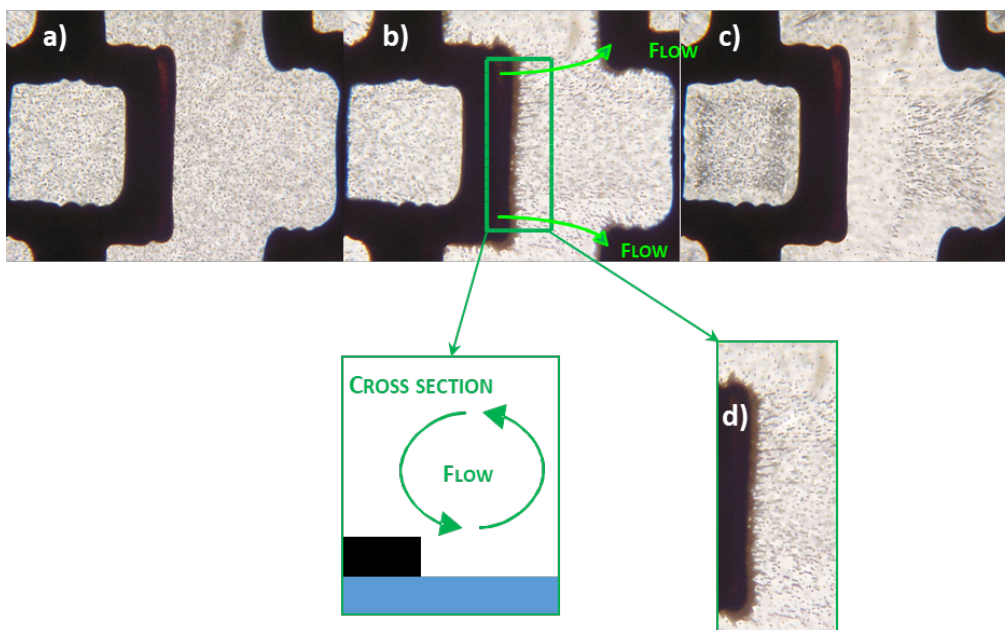


**Fig. S12** (a) Pictures of the bottom electrodes plane before polarization. Pictures of the bottom electrodes plane after 60s polarization at 20  $V_{pp}$  at (b) 10 MHz and (c) 2 kHz of PS particles ( $\phi = 1 \mu\text{m}$ ). (d) zoom on an area where EOF occurs.

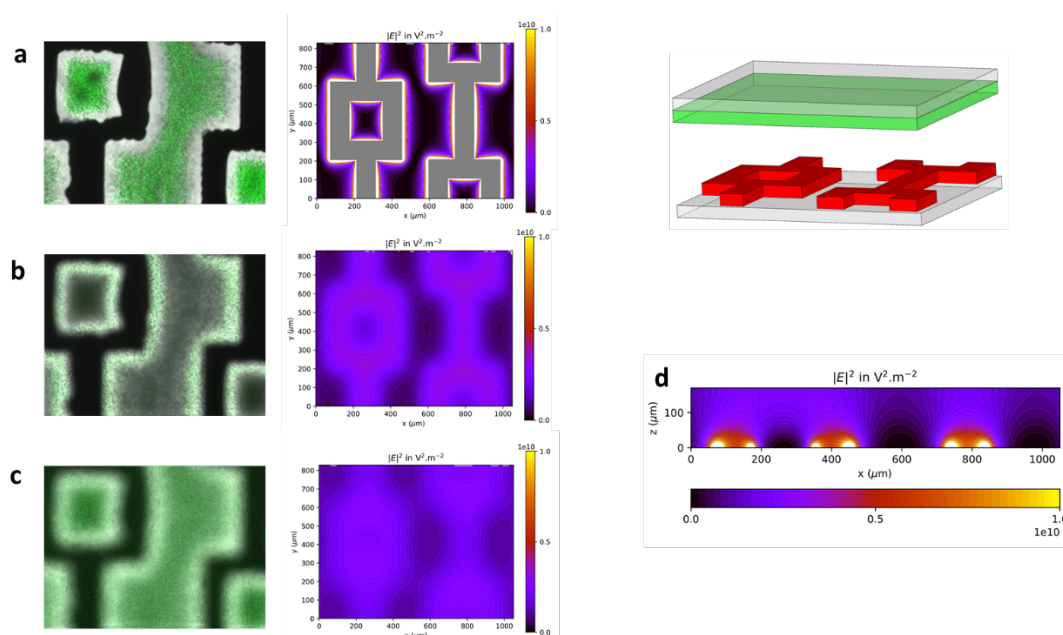


**Fig. S13** (left) Pictures after 60s polarization at 20  $V_{pp}$  (10 MHz) of PS particles ( $\phi = 1 \mu\text{m}$ ) and (right) the corresponding  $E^2$  distribution in the  $(x, y)$  planes at (a)  $z=0$ , (b)  $z=1/2$  and (c)  $z=1$ . (d)  $E^2$  distribution in the  $(x, z)$  plane at  $y = 1/2$ .

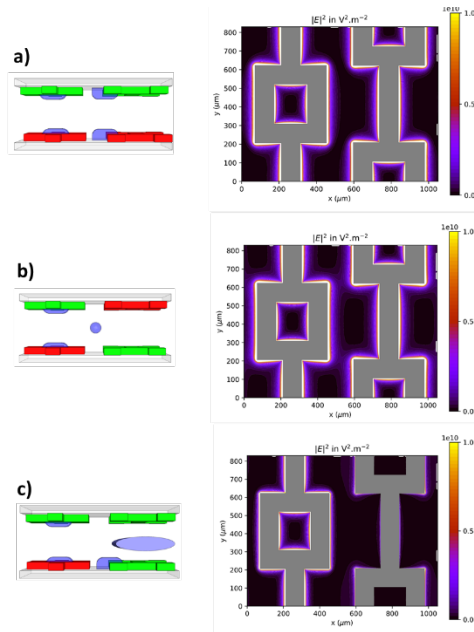


**Fig. S14** Distribution of  $E^2$  in top  $(x, y)$  plane ( $z=1$ ) for the configurations (a) 3, (b) 4 and (c) 5.

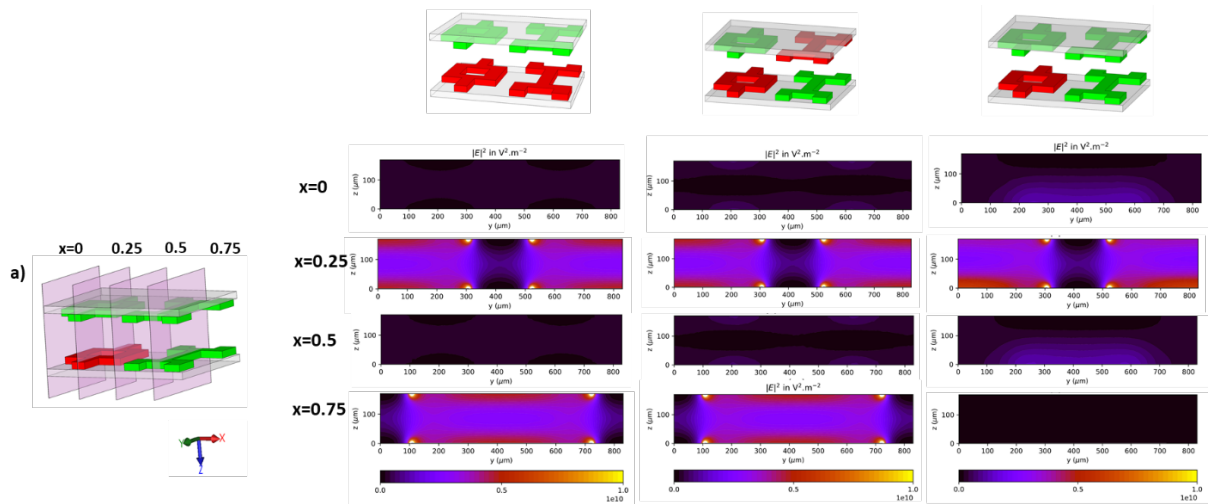


**Fig. S15:** Distribution of  $E^2$  in the  $(x, z)$  planes at different position in the channel ( $y$ -position) for the configurations (left) 3, (middle) 4 and (right) 5.

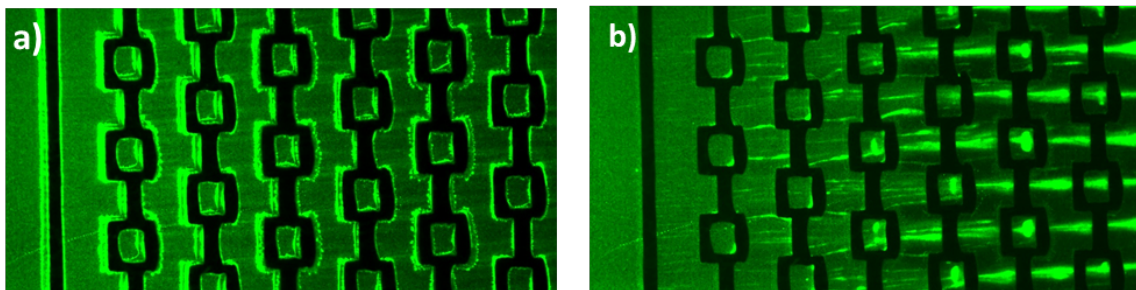


**Fig. S16:** Pictures after 60s polarization at 20  $V_{pp}$  of PS particles ( $\varnothing = 0.5 \mu\text{m}$ ) at (a) 100 kHz (pDEP) and (b) 10 MHz (nDEP).

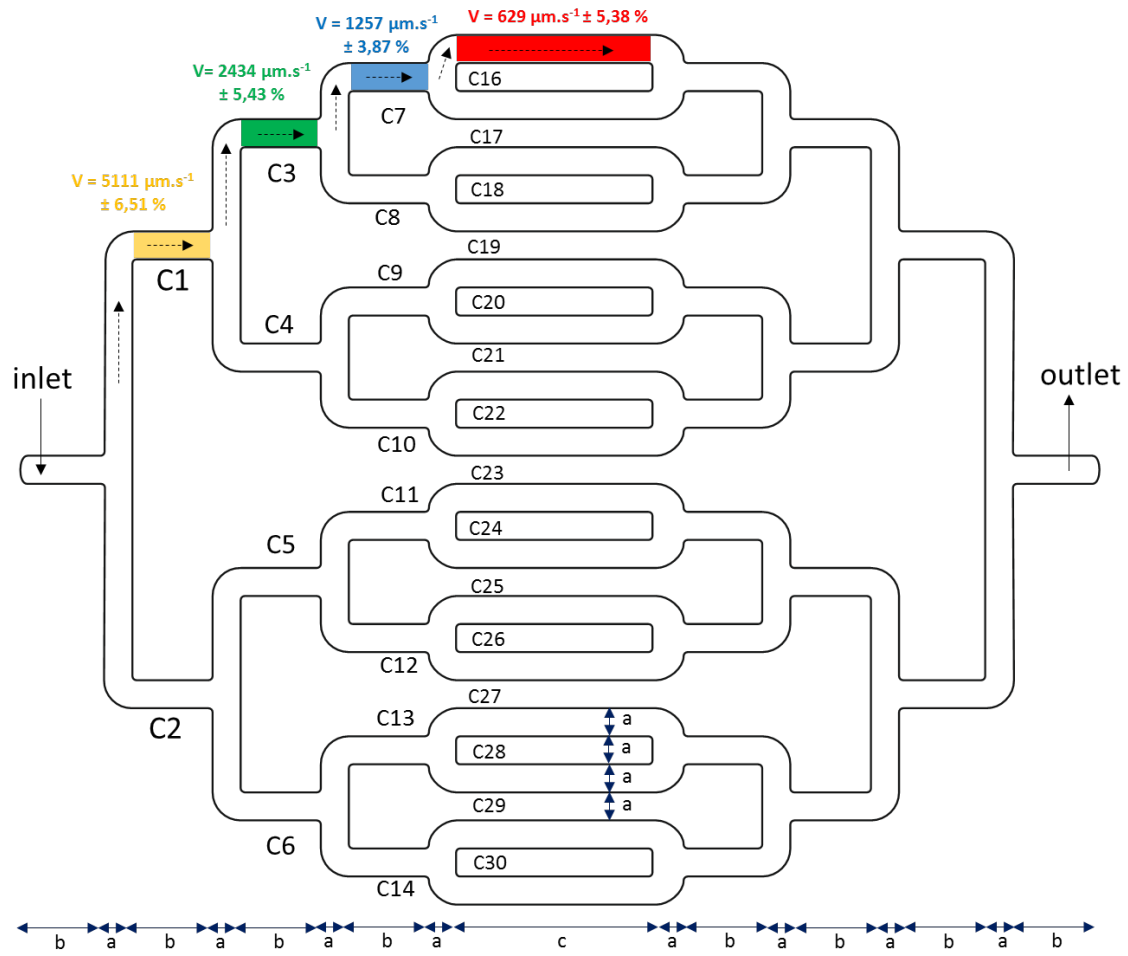


**Fig. S17:** Scheme of the microfluidic device showing the flow rate in each channel. Flow rates were estimated from analysis of at least 3 movies/channel, showing circulating fluorescent PS particles in C1 & C2, C3 & C4, C7 to C10 and C15 to C29.  $a=2,8\text{mm}$ ,  $b=8\text{mm}$ ,  $c=20\text{mm}$ . Total dimension is  $l=112\text{mm}$ ,  $L=92,4 \text{ mm}$ .